

Effect of grain constraint on the field requirements for magnetocaloric effect in Ni₄₅Co_xMn_{45-x}Sn₁₀ melt-spun ribbons

N. M. Bruno,^{1,2} Y. J. Huang,³ C. L. Dennis,⁴ J. G. Li,³ R. D. Shull,⁴ J. H. Ross, Jr.,^{1,5}
Y. I. Chumlyakov,⁶ and I. Karaman^{1,2,a)}

¹Department of Materials Science and Engineering, Texas A&M University, College Station, Texas 77843, USA

²Department of Mechanical Engineering, Texas A&M University, College Station, Texas 77843, USA

³School of Materials and Engineering, Shanghai Jiao Tong University, Shanghai 200240, People's Republic of China

⁴Materials Science and Engineering Division, Material Measurement Laboratory, National Institute of Standards and Technology, Gaithersburg, Maryland 20899, USA

⁵Department of Physics and Astronomy, Texas A&M University, College Station, Texas 77843, USA

⁶Siberian Physical Technical Institute, Tomsk State University, Tomsk 634050, Russia

(Received 4 June 2016; accepted 22 July 2016; published online 18 August 2016)

The influence of grain constraint on the magnetic field levels required to complete the isothermal martensitic transformation in magnetic shape memory alloys has been demonstrated for a NiCoMnSn alloy, and the magnetocaloric performance of an optimally heat treated alloy was quantified. Ni₄₅Co_xMn_{45-x}Sn₁₀ melt spun ribbons with $x = 2, 4, 5,$ and 6 were characterized. The $x = 5$ sample was determined to exhibit the lowest transformation thermal hysteresis (7 K) and transformation temperature range during transformation from paramagnetic austenite to non-magnetic martensite, as well as a large latent heat of transformation ($45 \text{ J kg}^{-1} \text{ K}^{-1}$). For this composition, it was found that increasing the grain size to thickness ratio of the ribbons from 0.2 to 1.2, through select heat treatments, resulted in a decrease in the magnetic field required to induce the martensitic transformation by about 3 T due to the corresponding reduction in the martensitic transformation temperature range. This decrease in the field requirement ultimately led to a larger magnetocaloric entropy change achieved under relatively smaller magnetic field levels. The giant inverse magnetocaloric effect of the optimized alloy was measured and showed that up to $25 \text{ J kg}^{-1} \text{ K}^{-1}$ was generated by driving the martensitic transition with magnetic fields up to 7 T. *Published by AIP Publishing.* [<http://dx.doi.org/10.1063/1.4960353>]

I. INTRODUCTION

Off-stoichiometric Heusler compounds, which exhibit magnetic field-induced martensitic transformations (MTs), have recently drawn considerable attention for magnetic refrigeration.¹⁻⁷ These include NiMnX (X = In, Sn, Sb) based metamagnetic shape memory alloys (MMSMAs), which exhibit a large latent heat during reversible MT.^{1,8} In the course of the field-induced MT, the latent heat of transformation gives rise to a magnetocaloric effect (MCE) upon the transformation from the weakly magnetic martensite into either a ferromagnetic⁹ or paramagnetic¹⁰ austenite. The inability to reversibly transform MMSMAs under small magnetic fields hinders its applicability for solid-state refrigeration.

Some of the reasons behind the high magnetic field requirements for the completion of MT in MMSMAs are relatively strong energy barriers against MT, and dissipative processes accompanying the transformation and phase front motion due to the incompatibility between the transforming phases.¹¹⁻¹³ The compatibility between the transforming phases can be controlled, to a certain extent, by chemistry modifications;¹⁴⁻¹⁶ however, chemical changes will also affect other MT characteristics, such as transformation temperatures,

which can sometimes be undesirable. Another possibility to manipulate the transformation barriers and dissipative processes is through microstructural control via grain size (GS) modifications, second phase particle formation, control over the degree of crystallographic order, etc.¹⁷⁻²¹ Thus, one of the goals of the present work is to reveal the effect of grain constraints on the field-induced MT in MMSMAs.

In a previous work,²² we introduced a detailed methodology for computing the field levels needed to achieve a reversible field-induced MT using the basic MT characteristics such as MT temperatures and their dependence on the applied magnetic field. To better understand the influence of microstructural modifications on these field levels in the present work, it is important to first briefly describe this methodology. In MMSMAs, the isothermal magnetic field-induced transformation from martensite to austenite is completed by applying $\mu_0 H_{comp}^{iso}$ at the martensite finish temperature, M_f . Assuming the response is linear, $\mu_0 H_{comp}^{iso}$ can be computed as²²

$$\mu_0 H_{comp}^{iso} = (A_f - M_f) \cdot \mu_0 dH^{A_f} / dT, \quad (1)$$

where μ_0 is the permeability of free space, A_f is the austenite finish temperature, and $\mu_0 dH^{A_f} / dT$ is the inverse rate of change of the austenite finish temperature as a function of applied field. Upon removing $\mu_0 H_{comp}^{iso}$ from the field-stabilized austenite phase at M_f , the MMSMA will completely

^{a)}Author to whom correspondence should be addressed. Electronic mail: ikaraman@tamu.edu

transform to its original martensitic state. For example, this process is illustrated for a transformation between a weakly magnetic martensite and a ferromagnetic austenite in Fig. 1, where the process follows the dotted line at M_f .

In Fig. 1, the magnetization vs. temperature histories of an example NiCoMnSn MMSMA are shown under a relatively small field, 0.05 T, and a large field chosen so that $7\text{ T} \geq \mu_0 H_{comp}^{iso}$. Under 0.05 T, the MMSMA exhibits a sharp change in magnetization upon heating, from the weakly magnetic martensite to the ferromagnetic austenite,²² and thermal hysteresis indicative of the MT. Applying a larger magnetic field results in a leftward shift of all MT temperatures at a rate proportional to $\mu_0 dH^{A_f}/dT$. $\mu_0 H_{comp}^{iso}$ is then identified as the field which makes A_f decrease until it is equal to the M_f temperature (e.g., at the field $\mu_0 H_2$ in Fig. 1, $A_f^{\mu_0 H_2} = M_f$). Clearly, reducing $A_f - M_f$ will reduce $\mu_0 H_{comp}^{iso}$ per Eq. (1), assuming that the magnetic field does not affect the transformation width and thermal hysteresis ($A_f - M_f$).

It should be noted that $A_f - M_f$ spans both the structural transition itself and the thermal hysteresis, $A_f - M_f = \Delta T_{elas} + \Delta T_{hys}$, where ΔT_{elas} is the structural transition range and ΔT_{hys} is the thermal hysteresis. ΔT_{elas} is defined by the over (under) heating (cooling) needed to overcome the elastic energy stored in the microstructure across the transition. These terms are defined using the MT temperatures as $\Delta T_{elas} = [\frac{M_s - M_f}{2} + \frac{A_f - A_s}{2}]$ and $\Delta T_{hys} = [\frac{A_f + A_s}{2} - \frac{M_s + M_f}{2}]$, where the s subscripts designate start temperatures.²²⁻²⁴

In this study, we attempt to keep ΔT_{hys} constant and change the microstructure with selected heat treatments to investigate the role of microstructure on ΔT_{elas} . We aim to elucidate microstructural factors that reduce $A_f - M_f$, and thus, $\mu_0 H_{comp}^{iso}$. ΔT_{hys} across MT is influenced by crystallographic ordering in some NiCoMnIn MMSMAs, which can be controlled by simple heat treatments,^{25,26} however, in

most NiCoMnSn MMSMA compositions, the long range crystallographic (B2 vs. L2₁) ordering is stable across a wide temperature range.²⁷⁻²⁹ This provides the means to keep ΔT_{hys} nearly constant after heat treatments that neither cause significant changes in crystallographic order nor form second phase particles in NiCoMnSn MMSMAs, but lend the ability to tune ΔT_{elas} by controlling the grain size.

NiCoMnSn MMSMA compositions in this study were, thus, pre-selected with small ΔT_{hys} to reveal the role of grain boundary constraints on ΔT_{elas} and the $\mu_0 H_{comp}^{iso}$ parameter given in Eq. (1) by controlling the grain size via grain growth through annealing. Here, we determine ΔT_{elas} in samples containing different degrees of grain constraint and relate the transformation characteristics to the magnetic field requirements for MT. Additionally, isothermal magnetic measurements are employed to compute the giant inverse MCE in the optimally annealed alloy.

II. EXPERIMENTAL DETAILS

Four samples of nominal compositions Ni₄₅Mn_{45-x}Co_xSn₁₀ with $x=2, 4, 5$, and 6 were synthesized via arc melting. Prior to melting the alloys, the arc furnace was first evacuated to a pressure of 0.13 Pa (10^{-3} Torr) and flushed 3 times in high purity argon. After flipping and re-melting the buttons at least 4 times to promote homogeneity, the melted buttons were suction cast into 5 mm diameter rods. The alloys were again re-melted in a vacuum melt spinner using an induction coil surrounding a quartz nozzle holding the alloy rod. The melted rod was then ejected via a small argon pressure onto a rotating copper wheel spinning with a surface speed of 17 m s^{-1} . Melt spinning resulted in approximately $30\text{ }\mu\text{m}$ thick ribbons of various lengths and widths.

The compositions of the melt spun ribbons were determined using wavelength dispersive spectroscopy (WDS) with a CAMECA SX-50 electron microprobe system.³⁰ The ribbon compositions were measured to be Ni_{44.50±0.15}Mn_{43.00±0.20}Co_{1.90±0.02}Sn_{10.70±0.07}, Ni_{44.40±0.35}Mn_{40.90±0.29}Co_{4.00±0.08}Sn_{10.80±0.03}, Ni_{44.40±0.08}Mn_{39.80±0.12}Co_{5.10±0.03}Sn_{10.80±0.07}, and Ni_{44.50±0.15}Mn_{39.30±0.21}Co_{5.40±0.06}Sn_{10.80±0.04}. Henceforth, these alloys are abbreviated as Co2, Co4, Co5, and Co6, respectively, or in some cases, by their nominal compositions.

Differential scanning calorimetry (DSC) was performed on the ribbon samples using a TA Instruments Q20 calorimeter.³⁰ The temperature was swept at 5 K min^{-1} between 353 K and 453 K. The MT temperatures (M_s , M_f , A_s , and A_f) were extracted from the measurements as demonstrated on the Co5 cooling curve in Fig. 2, where the cooling curves of each as-spun sample are shown. Lines were extrapolated from linear responses in the thermogram on either side of the martensitic transformation, and their intersections indicated the transformation temperatures. The Co5 ribbons were selected for the grain size study due to their lowest ΔT_{hys} (7 K) and largest latent heat of transformation. The entropy changes across the MT were computed, with the heat capacity, C_p , using $\Delta S_{tr} = \int_{M_f}^{M_s} \frac{C_p}{T} dT$ and the results shown in Fig. 2, to be 42, 41, 45, and 42 J kg⁻¹ K⁻¹ for the Co2, Co4, Co5, and Co6 samples, respectively. These are nearly 4 times the values first

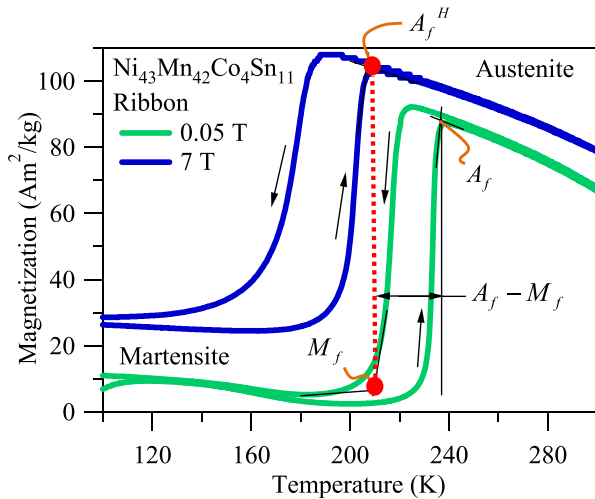


FIG. 1. The magnetization vs. temperature response of the Ni₄₃Mn₄₂Co₄Sn₁₁ ribbons under magnetic fields of $\mu_0 H_1 = 0.05\text{ T}$ and $\mu_0 H_2 = 7\text{ T}$ with the MT temperatures indicated as a function of applied field (A_f : austenite finish temperature under 0.05 T, A_f^H : austenite finish temperature under 7 T, and M_f : martensite finish temperature at 0.05 T). The dotted line indicates the isothermal loading path between pure martensite and pure austenite. This figure demonstrates that NiCoMnSn is capable of existing at both martensite and austenite at M_f depending on the applied field.

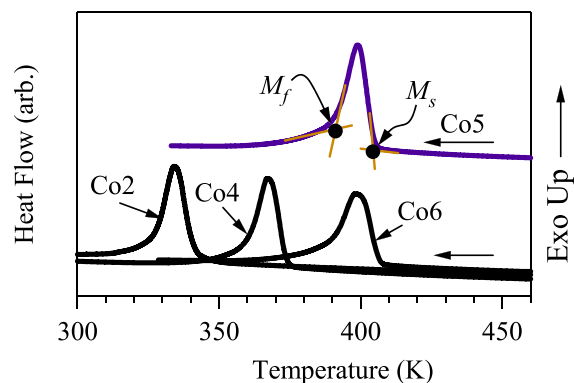


FIG. 2. DSC results of as-spun ribbons on cooling from austenite to martensite for different compositions of $\text{Ni}_{45}\text{Mn}_{45-x}\text{Co}_x\text{Sn}_{10}$ with $x = 2, 4, 5,$ and 6 . A vertical offset has been added to the $x = 5$ sample DSC results for clarity, and lines were drawn to demonstrate how the martensitic transformation temperatures can be determined from the thermograms.

reported in this alloy composition range,³¹ indicating that these alloys are strong candidates for MCE applications. Furthermore, the field-free thermal hysteresis values computed from DSC thermograms were 11.4 K, 11.4 K, 7 K, and 8.1 K, respectively.

To promote the grain growth, some Co5 ribbons were annealed at 1073 K for durations of 30 min, 60 min, 90 min, 120 min, and 600 min; at 1173 K for 20 min, 40 min, 60 min, 80 min, 100 min, and 120 min; and at 1198 K for 30 min, 60 min, and 120 min. The samples were annealed in a partial argon atmosphere (5 Torr) within quartz tubes and furnace cooled (FC) after annealing to produce consistent crystallographic ordering and vacancy concentration among the samples. The ribbon microstructures were investigated using a FEI Quanta 600 field-emission scanning electron microscope (SEM).³⁰ Backscatter (BSE) and secondary electron (SE) detectors were used to obtain images of the grains on the ribbon face and ribbon cross sections after cleaving them transversely.

The sizes of at least 500 grains were measured from BSE images of the ribbon faces. Grain areas were computed using Scion Image,³⁰ and the areas were then converted to diameters of the equivalent circle areas. A histogram of grain diameters was plotted using a bin size of $1\ \mu\text{m}$, and a Gaussian curve was fit to the data. Thus, the maxima of the fitted Gaussian peaks corresponded to the average grain diameters, referred to herein as grain size (GS). The standard deviation of the Gaussian curves was used to determine the degree of error in the reported GS . The ribbon thicknesses (t) were also measured from the SE images, so that the GS to thickness ratio (GS/t) could be used as a measure of grain constraint as defined in previous reports on the thermomechanical coupling of shape memory alloys (SMAs).^{32,33}

Finally, the magnetic properties of the ribbons were measured using a Quantum Design SQUID-VSM magnetometer³⁰ with a high temperature oven. The ribbons were mounted on a heater stick with copper foil under vacuum ($<1\ \text{mPa}$ or $<0.01\ \text{mT}$) and were locally heated using an electrical current through the heater stick at $1\ \text{K}\ \text{min}^{-1}$ across the martensitic transition (from 323 K to 573 K) under constant applied magnetic fields of 0.05 T, 1 T, 3 T, 5 T, and 7 T

with a temperature step size of 5 K while their magnetization (M) was measured. After the M vs. T data collection, magnetic isotherms (M vs. $\mu_0 H$) were also measured in increments of 3 K with increasing temperature across the martensitic transition, and these data were used to compute the magnetic field induced entropy change. During these measurements, the magnetic field was slowly ramped at $\approx 2.8\ \text{kA}\ \text{m}^{-1}\ \text{s}^{-1}$ ($35\ \text{Oes}^{-1}$) to ensure that the MMSMA did not change temperature as a result of the magnetic field induced phase transformation and adiabatic heating. At temperatures where the applied field resulted in a partial magnetic field induced transformation, the MMSMA was cooled to its martensitic state under zero field prior to performing the next highest isothermal incremental measurement. This procedure is known as discontinuous heating and prevented erroneously large entropy changes from the post-processing in the magnetization data as described elsewhere.^{22,34–36}

III. RESULTS AND DISCUSSION

A. Grain size and martensitic transformation temperatures

Average grain size for each annealing treatment was determined in Co5 ribbons using the methods described in Section II. Fig. 3(a) shows normalized grain size distributions and their fitted Gaussian curves for minimum and maximum annealing durations at each annealing temperature. Grain distributions are not shown for the maximum annealing duration for clarity. At higher annealing temperatures,

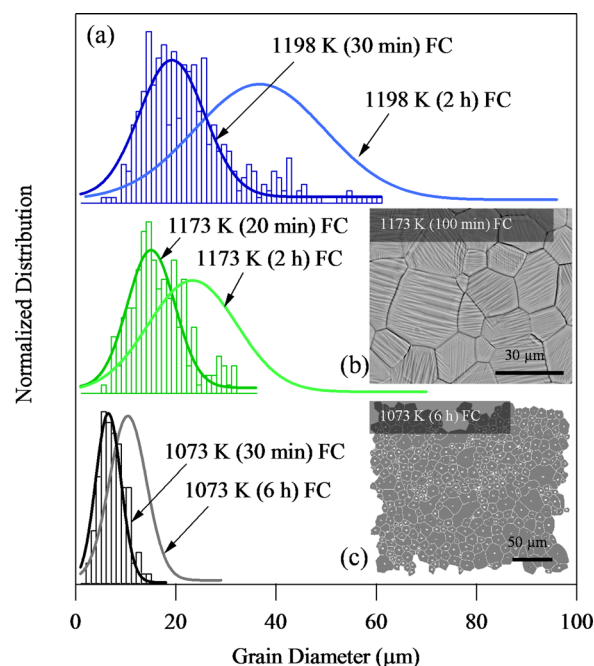


FIG. 3. Normalized grain distributions for the minimum annealing durations and the corresponding fitted Gaussian curves for minimum and maximum annealing durations at 1198 K, 1173 K, and 1073 K annealing temperatures in $\text{Ni}_{45}\text{Co}_5\text{Mn}_{40}\text{Sn}_{10}$ (a). The maximum of the fitted Gaussian peaks was interpreted as the average grain size for a given annealing treatment. An example backscattered electron micrograph for the 1173 K 100 min annealing treatment followed by furnace cooling is shown in (b). Actual grain areas were computed using Scion Image³⁰ by isolating the grains (c), and their size distribution was then plotted in (a).

the average grain size (peak of the Gaussian curve) was increased. Additionally, longer duration treatments at the same annealing temperature led to an increase in curve width and corresponding peak grain diameter. Fig. 3(b) is an example micrograph for the 1173 K 100 min FC annealing case that was used to extract grain diameter data using Scion Image.³⁰ Grains were isolated using the software, as depicted in Fig. 3(c), and grain areas were then extracted and converted to grain diameters.

Fig. 4 shows the BSE and SE micrographs of the ribbon faces and cross-sections for the 1073 K, 1173 K, and 1198 K (2 h) heat treatments. Clearly, annealing the ribbons at 1073 K was not sufficient to promote grain growth to an extent large enough for the grains to completely extend through the ribbon thickness. On average, the *GS* of the 1073 K annealed ribbons

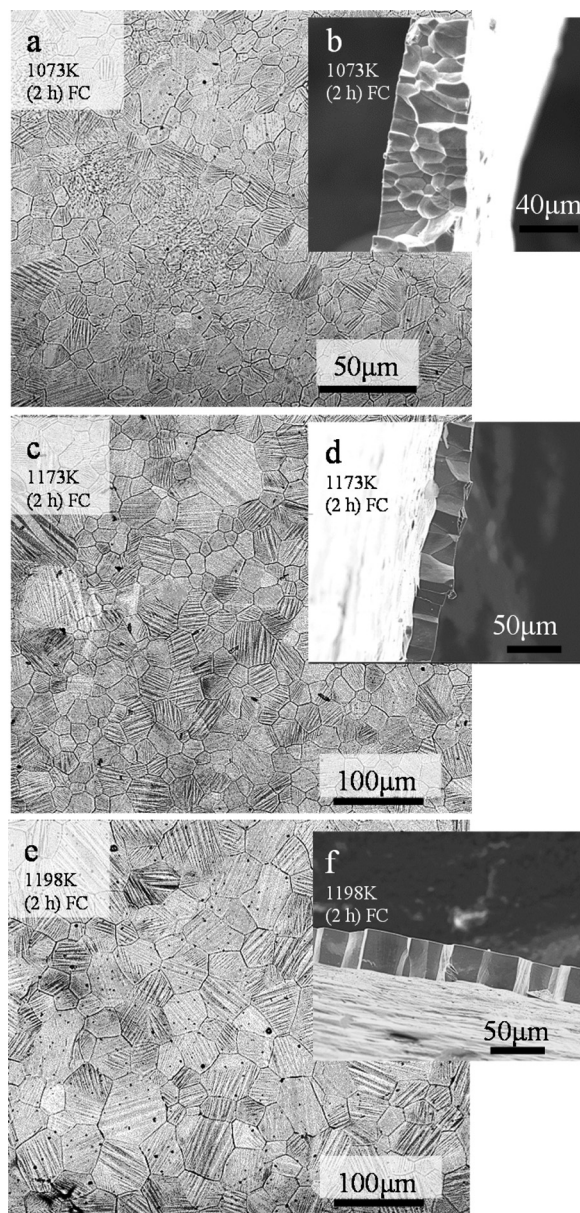


FIG. 4. Backscattered ((a)–(c)–(e)) and secondary ((b)–(d)–(f)) electron images of $\text{Ni}_{45}\text{Co}_5\text{Mn}_{40}\text{Sn}_{10}$ ribbons after annealing and furnace cooling from 1073 K (a) and (b), 1173 K (c) and (d), and 1198 K (e) and (f) for 2 h.

was $8.1 \mu\text{m}$, while the ribbon thicknesses were about $30 \mu\text{m}$ as verified by cleaved cross-sections studied with SE imaging. The annealing treatments for 2 h at 1173 K and 1198 K were sufficient for the grains to grow completely through the thickness. Differences in grain sizes are observable between the different annealing treatments in Fig. 4.

DSC measurements were performed on the Co5 ribbons in order to identify the MT temperatures pre- and post-annealing. The average measured grain sizes and the corresponding M_s temperatures are plotted in Fig. 5 for all heat treated ribbons. In the figure, M_s marginally increases with annealing time and temperature, i.e., with grain diameter, and changes the slope around 414 K corresponding to a grain size of nearly $30 \mu\text{m}$. Interestingly, the thickness of the ribbon is nearly $30 \mu\text{m}$. A notable change in slope is observed in the M_s temperature as the grain size reaches the thickness of the ribbon. The error bars in Fig. 5 indicate the standard error (2σ) obtained for the fitted grain sizes described earlier.

B. Effect of microstructurally stored elastic energy

To better understand the role of MMSMA microstructure on magnetic field levels for the fully reversible martensitic transformation, we must first clarify how microstructural features influence the energetics of the MT. In the theory of MT, the local free energy balance for the forward MT is written as^{37,38}

$$\Delta\psi_{chem}^{A\rightarrow M} + \Delta\psi_{elas}^{A\rightarrow M} + E_{irr} = 0, \quad (2)$$

where $\Delta\psi_{chem}^{A\rightarrow M}$ is the chemical free energy difference between austenite and martensite, $\Delta\psi_{elas}^{A\rightarrow M}$ is the microstructurally stored elastic energy across the martensitic transition (ΔT_{elas}), and E_{irr} is the dissipated energy generated from the transformation. With the absence of the second and third terms in Eq. (2), the transformation would be an ideal first order phase transformation at temperature T_0 , where $T_0 = (A_f + M_s)/2$.³⁸ Both $\Delta\psi_{elas}^{A\rightarrow M}$ and E_{irr} terms lead to deviations from the ideal response. Following these basic descriptions, we build most of our discussion pertaining to

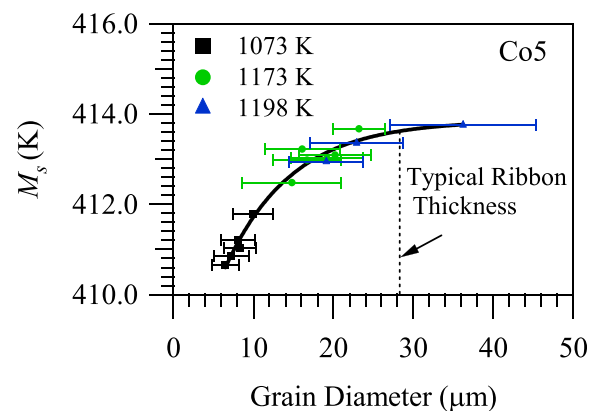


FIG. 5. The martensitic start temperature, M_s , under zero field for various grain diameters in the Co5 samples after promoting grain growth via annealing. A vertical dashed line represents the typical (average) ribbon thickness in the melt spun ribbons. Error bars indicate \pm one standard deviation from the Gaussian regression of the grain size data.

the effect of grain size on ΔT_{elas} and ΔT_{hys} parameters in annealed MMSMAs.

As defined in Refs. 23, 24, and 37, $\Delta\psi_{elas}^{A\rightarrow M}$ can be fundamentally expressed as $0.5 \cdot \Delta S_{tr}(M_s - M_f)$ for the austenite to martensite transformation. Here, we average the forward and reverse transformation temperature ranges with ΔT_{elas} and therefore compute the $\Delta\psi_{elas}^{A\rightarrow M}$ term in Eq. (2) with $0.5 \cdot \Delta S_{tr} \Delta T_{elas}$. This value is an indication of how much elastic strain energy must be overcome to transform MMSMAs. In MCE applications, the elastic strain energy stored through the transformation is overcome by applying magnetic fields. Reducing $\Delta\psi_{elas}^{A\rightarrow M}$ ultimately reduces the required magnetic field level needed to expose the full potential giant MCE.

To better compare the heat treated alloys in this study, $\Delta\psi_{elas}^{A\rightarrow M}$ was normalized with the latent heat of the martensitic transformation.³⁷ As such, the ratio of $\Delta\psi_{elas}^{A\rightarrow M}/Q_{tr}$ was employed, where Q_{tr} is the latent heat of the MT, $Q_{tr} = \Delta S_{tr} M_s$.¹³ Then, $\Delta\psi_{elas}^{A\rightarrow M}/Q_{tr}$ can be computed as $\frac{0.5 \cdot \Delta T_{elas}}{M_s}$. Conveniently, this ratio eliminates the need to quantify the entropy change across the MT but gives a relative comparison of energy storage between different MMSMAs with different microstructural conditions. The ratio $\Delta\psi_{elas}^{A\rightarrow M}/Q_{tr}$ was computed for various GS/t conditions, and the ramifications concerning the required magnetic field for a full transformation (see Eq. (1)) are discussed below.

We found that $\Delta\psi_{elas}^{A\rightarrow M}/Q_{tr}$ decreases with increasing annealing temperature and heat treatment duration. For example, ribbons annealed for 120 min at 1073 K exhibited a $\Delta\psi_{elas}^{A\rightarrow M}/Q_{tr}$ ratio of 1.05, whereas the $\Delta\psi_{elas}^{A\rightarrow M}/Q_{tr}$ ratio of those annealed for 120 min at 1198 K was only 0.80. This parameter decreases with increasing grain size indicating a smaller amount of strain energy was stored in the larger grains. Smaller grains offer more nucleation sites for martensite and, therefore, lead to a higher density of transformation interfaces and higher stored elastic strain energy.¹³ This energy must then be overcome with a magnetic field to transform the MMSMA.

The energy dissipation, E_{irr} , on the other hand, can be computed by the expression $E_{irr} = \Delta S_{tr} \Delta T_{hys}$.²³ Similarly, this property can be normalized with the latent heat of the MT, thus quantifying the fraction of energy lost to heat (not converted to MCE cooling) across MT and can be expressed as $E_{irr}/Q_{tr} = \Delta T_{hys}/M_s$. This value should be minimized through microstructural tuning to produce a favorable MCE. Not only will reduce this value amplify MCE cooling but also it will reduce the magnetic field levels required to transform the MMSMA by reducing $A_f - A_s$.

Although it was intended to keep dissipation, or ΔT_{hys} , constant by maintaining the crystallographic order in our samples, some small differences were still observed between different heat treatments. It was found that when ribbons were annealed for 30 min and 80 min at 1073 K and 1173 K, respectively, their E_{irr}/Q_{tr} ratio was 2.0. Annealing at higher temperatures, such as 1198 K for 60 min, resulted in a decrease in E_{irr}/Q_{tr} to 1.9. Larger grain sizes or high GS/t ratios seemed to only marginally reduce E_{irr}/Q_{tr} . Clearly, the E_{irr}/Q_{tr} ratio did not exhibit the same level of reduction with grain size increase as the $\Delta\psi_{elas}^{A\rightarrow M}/Q_{tr}$ ratio.

C. GS/t ratio vs. martensitic transition range

In Fig. 6, the $M_s - M_f$ and $A_f - A_s$ transition ranges are plotted as a function of GS/t ratio. They are shown to decrease with increasing GS/t up to 1.2. $M_s - M_f$ for the 1073 K heat treated ribbons was about 9 K. Increasing the annealing time at this temperature had a minor effect on $M_s - M_f$ and GS/t . The 2σ of the grain size, as apparent in Fig. 3 from the width of the peaks, also did not exhibit much change. GS/t was around 0.2 for the ribbons annealed at 1073 K. The low standard deviation in each ribbon annealed at 1073 K indicates that either the grains were at a size in which their surface energy was near an equilibrium or the atomic diffusivity was too slow. In this condition, each grain (with the exception of those on the ribbon surface) was completely in contact with its neighboring grains on all sides, as shown in Fig. 4(b). Thus, MT in these grains would produce a tendency for martensite to self-accommodate. The self-accommodation process produces many interacting martensite interfaces and stores elastic energy.¹³ In ribbons with longer and higher temperature annealing treatments, on the other hand, the larger grains are only in contact with their neighbors along their circumference as shown in Figs. 4(d) and 4(f). These grains exhibit two free surfaces where no interaction with neighboring grains could occur. Ultimately, larger martensite twins are observed in the SEM micrographs, and therefore, less interfaces are available for microstructural strain energy storage.

In the 1173 K samples, the standard deviation of the grain size distribution increased. This indicates that increasing annealing temperature did not promote growth in all grains, but that some grains grew at the expense of others (see Fig. 4(c)). The 1173 K heat treatments resulted in a decrease of $M_s - M_f$ with increasing GS/t between the range of $0.5 < GS/t < 0.7$ as shown in Fig. 6. A further decrease in $M_s - M_f$ was observed along with higher GS/t ratios, $0.7 < GS/t < 1.2$, after annealing at 1198 K. Although GS/t is less than unity for most cases in Fig. 6, all of the heat treatments at 1173 K and above promoted grain growth through the cross section, as shown in Figs. 4(d) and 4(f).

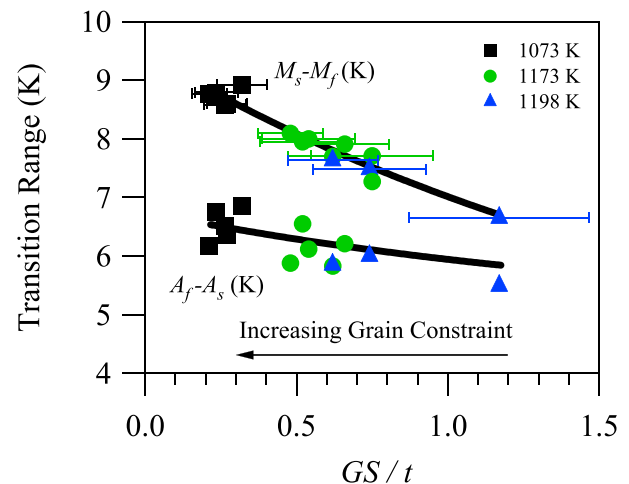


FIG. 6. Martensitic transition ranges as a function of grain size to thickness ratio in $\text{Ni}_{45}\text{Mn}_{40}\text{Co}_5\text{Sn}_{10}$ annealed ribbons. Error bars indicate \pm one standard deviation (σ) from the Gaussian regression of the grain size data.

As noted above, the grains did not easily grow to average diameters beyond the thickness of the ribbon. This phenomenon limited the achievable GS/t ratios to around 1. However, it is believed that longer annealing times might further increase the GS/t ratio, but at a slower rate. This potential increase, albeit minimal, should also further succeed in decreasing the martensitic transformation range and, in turn, reduce the required magnetic field levels needed for magnetic field induced transformation.

Finally, in Fig. 6, $A_f - A_s$ is not affected by grain size to the same extent as $M_s - M_f$ due to the strain energy recovered on the reverse martensite-to-austenite transformation.³⁷ However, there is a slight decrease, on average, in $A_f - A_s$ as GS/t increases. In addition, $A_f - A_s$ is always less than that of the forward transformation, $M_s - M_f$. It is believed that most of the stored elastic energy from the forward transition is recovered^{24,37} and therefore results in a smaller reverse transition range as observed here. Overall, decreasing $M_s - M_f$ and $A_f - A_s$ resulted in a smaller overall temperature range ($A_f - M_f$) that must be overcome to complete the transformation as discussed earlier using Eq. (1).

D. Magnetic behavior and magnetic-field induced phase transformation in large grain size ribbons

Decreasing $A_f - M_f$ temperature range via grain growth ultimately decreases the required magnetic field to complete the magnetic field induced transformation at M_f . In order to compute the magnetic field level in Eq. (1), iso field thermomagnetization curves were measured in the sample with the largest grain size, i.e., the optimized 1198 K (2 h) FC ribbons, which are depicted in Fig. 7(a). As shown in the figure, $\text{Ni}_{45}\text{Co}_5\text{Mn}_{40}\text{Sn}_{10}$ exhibits a small magnetic signal in the low temperature martensite phase of approximately 2 to 5 $\text{A m}^2 \text{ kg}^{-1}$ (emu/g) across a nearly 70 K temperature interval. On heating, a meta-magnetic transition occurs from the low temperature weakly magnetic martensite phase to the high temperature austenite phase. The start and finish of the martensite to austenite transformation are denoted by A_s and A_f , respectively, on the thermomagnetic response under 1 T in the figure.

The bulk austenite phase only exhibits magnetization up to 45 $\text{A m}^2 \text{ kg}^{-1}$ under an applied field of 7 T. This level of magnetization is comparable to other meta-magnetic SMAs, where austenite has been shown to be paramagnetic.^{10,39,40} Additionally, the lack of magnetic saturation in austenite at fields up to 7 T suggests that austenite is not ferromagnetic in our alloys, but rather paramagnetic, or a mixture of ferromagnetic and paramagnetic material.

Here, we performed a Curie-Weiss fit on the thermomagnetic data at temperatures above A_f to determine magnetic characteristics of the austenite phase. Magnetization data was fitted using the expression,

$$M = \frac{N_A}{3k_B} \mu_{eff}^2 \frac{(\mu_0 H)}{T - T_C} \times n, \quad (3)$$

where N_A is Avogadro's Number, k_B is the Boltzmann constant, $\mu_0 H$ is the applied field, T_C is the fitted austenite Curie temperature, n was assumed to be the number of moles of Mn

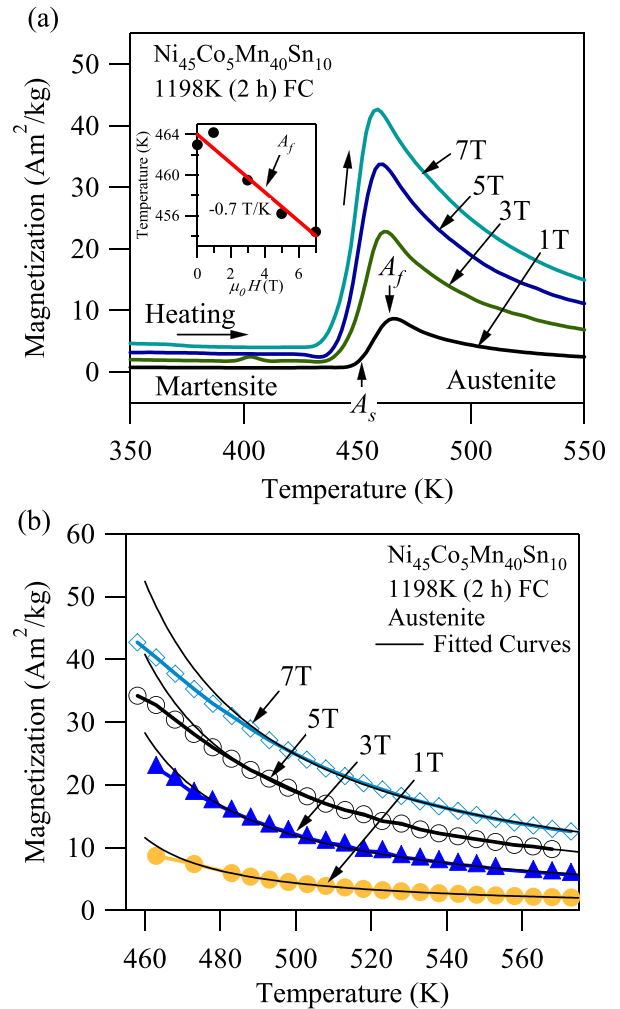


FIG. 7. Isofield thermomagnetization heating curves for $\text{Ni}_{45}\text{Co}_5\text{Mn}_{40}\text{Sn}_{10}$ 1198 K (2h) furnace cooled annealed ribbons (a) and the corresponding Curie-Weiss fitted curves in the high temperature Austenite phase (b). The A_f temperature versus applied field phase diagram is plotted in the inset of (a).

per gram-atom, and μ_{eff} is defined as $\mu_{eff} = g\mu_B\sqrt{J(J+1)}$. Here, μ_B is the Bohr magneton, g is the Lande' g-factor (assumed to be 2), and J was the fitted angular momentum. The influence of cobalt was neglected, and the magnetic order of the bulk alloy was assumed to only depend on the magnetic interactions of manganese (Mn) as demonstrated in previous works.^{9,10} The fitted curves are shown in Fig. 7(b) for each isofield measurement. Table I summarizes the A_f temperatures and the fitted magnetic properties in the NiCoMnSn annealed ribbons.

TABLE I. Austenite finish temperature and fitted magnetic properties of 1198 K (2h) annealed $\text{Ni}_{45}\text{Co}_5\text{Mn}_{40}\text{Sn}_{10}$ ribbons with $n = 45.73$ moles-Mn/gm-atom.

Applied field, $\mu_0 H$ (T)	T_C (K)	J	A_f (K)
1	436 ± 0.2	0.710 ± 0.001	464
3	431 ± 0.9	0.702 ± 0.006	462
5	426 ± 0.7	0.709 ± 0.004	460
7	424 ± 0.7	0.695 ± 0.003	458

Interestingly, J was found to be nearly 0.7 under all applied field levels, which is much less than the expected value of $gJ\mu_B = 4\mu_B$ (where the local moment would be carried by Mn only) measured in other Cobalt (Co)-free magnetic shape memory alloys.^{10,40,41} This suggests that the austenite phase exhibits itinerant magnetism where the angular momentum, J , depends on the interaction between Mn and Co. Since the thermomagnetic data fitted well to the Curie-Weiss formula, we characterize the austenite phase as paramagnetic with a Curie temperature of nearly 436 K under 1 T. The precise influence of Co on the magnetic order in the austenite phase, however, is obscured by the martensitic transformation as it prevents the measurement of the saturated magnetic moment in austenite (ground state magnetic moment) at low temperatures. Upon increasing the applied field, the Curie temperature experiences a decrease at a rate similar to the rate of decrease in the martensitic transformation temperature, or $dT/\mu_0 dH^{A_f}$, as tabulated in Table I.

Here, it is important to note that the rate at which the martensitic transformation temperatures decrease with the applied magnetic field, i.e. $dT/\mu_0 dH^{A_f}$, directly influences the $\mu_0 H_{comp}^{iso}$ described in Eq. (1). In MMSMAs where the austenite phase is paramagnetic, as in this study, $dT/\mu_0 dH^{A_f}$ is typically smaller than in MMSMAs with ferromagnetic austenite phases that exhibit a high change in magnetization at the martensitic transition.⁴² Therefore, it is expected that $\mu_0 dH^{A_f}/dT$ in Eq. (1) is elevated in our selected MMSMA composition when compared to MMSMAs with ferromagnetic austenite. Nevertheless, the low thermal hysteresis (7 K) in the selected composition was expected to compensate for the high $\mu_0 dH^{A_f}/dT$ and effectively reduces $\mu_0 H_{comp}^{iso}$. This interplay between thermal hysteresis and the $\mu_0 dH^{A_f}/dT$ parameter described in Eq. (1) should be taken into account in MMSMA selection or design. The work, herein, serves to demonstrate a microstructural method to reduce $\mu_0 H_{comp}^{iso}$, even in MMSMA compositions with paramagnetic austenite.

Fig. 8 depicts magnetic isotherms of pure martensite, austenite, and the magnetic field induced transformation. The non-linear low field (<1 T) behavior of martensite at 421 K, as shown in the inset, may suggest that the martensite is a mixture of magnetic phases.³¹ This has also been proposed for other meta-magnetic SMAs¹⁰ and is consistent with the previous reports of the $Ni_{45}Co_5Mn_{40}Sn_{10}$ alloy that report the existence of ferrimagnetism in the martensite phase.³¹ At 442 K, on the other hand, the magnetization level of austenite is clearly non-linear for the entire range of applied field up to 7 T, suggesting that the paramagnetic austenite should saturate at fields larger than 7 T. At 439 K, the magnetic field induced transformation occurs from martensite to austenite, and a magnetization increase of nearly 35 A m² kg⁻¹ was measured. However, the magnetization value reached at 439 K under 7 T is lower than the magnetization value that 100% austenite would result in, and thus, it is believed that application of a greater magnetic field would give rise to a larger increase in magnetization corresponding to a greater degree of martensitic transformation.

Using the iso-field thermo-magnetization curves in Fig. 7(a), a A_f vs. $\mu_0 H$ phase diagram was plotted in the inset. The slope of the martensite-austenite coexistence line yielded the

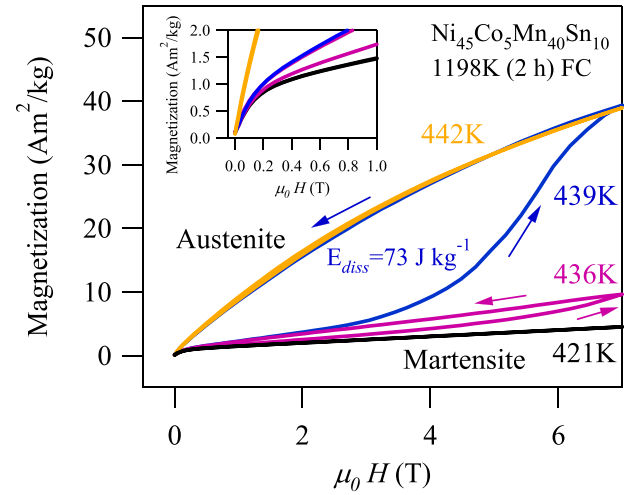


FIG. 8. Magnetic isotherms for $Ni_{45}Co_5Mn_{40}Sn_{10}$ 1198 K (2 h) furnace cooled annealed ribbons. The magnetization of the martensite as the magnetic field ($\mu_0 H$) was first increased and then decreased (indicated by arrows) is shown at 421 K, austenite at 442 K, and the partial meta-magnetic transformations at 439 K and 436 K. The inset shows the non-linear magnetic response in martensite at 421 K under 1 T applied field.

$\mu_0 dH^{A_f}/dT$ parameter needed in Eq. (1) and was determined to be nearly $-0.7 T K^{-1}$. Using this slope and Eq. (1), the magnetic field level needed to complete the MT at temperature M_f was plotted in Fig. 9, thus explaining the incomplete magnetic field induced transformation in Fig. 8 at 439 K. As shown in Fig. 9, approximately 9.6 T is required for a GS/t ratio of 1.2 in these ribbons to complete the martensitic transformation. It can be seen that decreasing $A_f - M_f$ by only a few Kelvin also decreases the magnetic field requirement by approximately 3 T. The samples with GS/t close to 0.32 would require about 12.5 T to complete the reversible magnetic field induced transformation, while those with GS/t ratios near 0.62 and 1.2 required fields of about 11 T and 9.5 T, respectively.

Reducing the required field by 3 T is significant as it would require substantially lower magnetic energy to transform the MMSMA and is a pathway to use permanent magnets for solid-state refrigeration. Although the lowest field

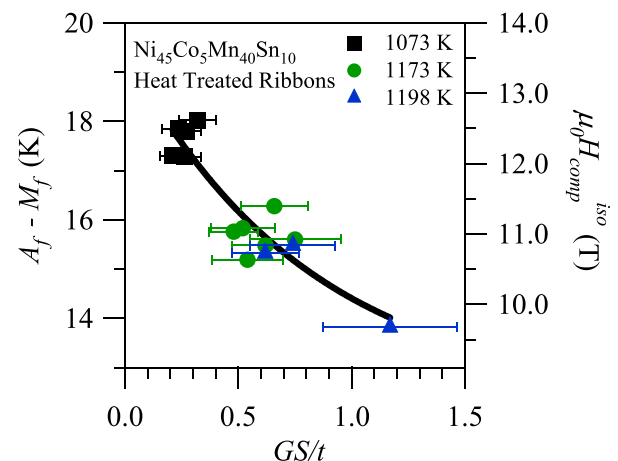


FIG. 9. $A_f - M_f$ and $\mu_0 H_{comp}^{iso}$ dependencies on grain size to thickness ratio (GS/t) in $Ni_{45}Co_5Mn_{40}Sn_{10}$ annealed ribbons. Error bars indicate \pm one standard deviation from the Gaussian regression of the grain size data.

capable of completely transforming the MMSMA in this study was computed to be 9.5 T, about 7.5 T larger than permanent magnet capabilities, reducing the magnetic field requirements using carefully selected heat treatments to control the microstructure will allow a larger fraction of the transformation to occur with low-field cycling and, in turn, increase the low-field refrigerant capacity of the MMSMA.⁷

E. Giant MCE in large grain size ribbons

The magnetic isotherms in Fig. 8 were measured from 400 K to 472 K in increments of 3 K using the discontinuous heating procedure as described in the experimental details. As shown in Fig. 8, the meta-magnetic field-induced transformation began around 3 T at 439 K, as indicated by the increase in magnetization from the nearly linear response of the martensite's magnetization to the applied field. The magnetization level continuously increased as the transformation progressed to austenite. On removing the magnetic field, a magnetic hysteresis was observed. The alloy dissipates nearly 73 J kg^{-1} (calculated using the area between the field loading and unloading curves), which is low in comparison to other meta-magnetic SMAs^{22,42} and can be attributed to this alloy's particularly small thermal hysteresis.

Magnetic isotherms, M vs. $\mu_0 H$, were integrated using the traditional expression^{3,22}

$$\Delta S_{mag}(T_K, 0 \rightarrow \mu_0 H) = \frac{\mu_0}{\Delta T_k} \int_0^H (M_{T_{k+1}} - M_{T_k}) dH, \quad (4)$$

where T_k is an isothermal test temperature, $\Delta T_k = (T_{k+1} - T_k)$, and $T_K = (T_{k+1} + T_k)/2$. Employing Eq. (4), the temperature dependent magnetic field induced entropy change was computed as shown in Fig. 10. A positive entropy change is generated by applying a magnetic field to the martensite in $\text{Ni}_{45}\text{Co}_5\text{Mn}_{40}\text{Sn}_{10}$ annealed ribbons near the martensitic transition temperature, nearly zero entropy change is produced from the martensite phase far below the transformation temperature (left of diagram), and a negative entropy change is produced by applying a magnetic field to the austenite phase (right of diagram). The magnitude of the entropy change generated by the martensitic transformation is dependent on the extent of martensitic transition that occurs by applying the magnetic field.^{22,42}

As shown above, the total entropy change that can be achieved in this alloy, as measured with differential scanning calorimetry, was found to be $45 \text{ J kg}^{-1} \text{ K}^{-1}$. Here, only $27 \text{ J kg}^{-1} \text{ K}^{-1}$ is produced from applying 7 T, $22 \text{ J kg}^{-1} \text{ K}^{-1}$ from applying 5 T, $10 \text{ J kg}^{-1} \text{ K}^{-1}$ from applying 3 T, and only $2 \text{ J kg}^{-1} \text{ K}^{-1}$ from applying a 1 T field. According to Eq. (1) and the magnetic field levels shown in Fig. 9, the complete $45 \text{ J kg}^{-1} \text{ K}^{-1}$ can be generated with a magnetic field of nearly 9.6 T at the M_f temperature. For the other annealed ribbons with a higher degree of grain constraint ($GS/t < 1$), magnetic fields larger than 10.5 T are needed to generate the same magnitude of entropy change, thus showing the importance of the degree of grain constraint and

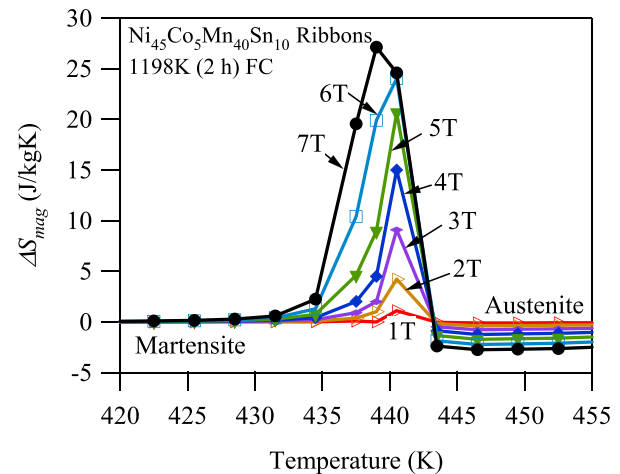


FIG. 10. The entropy change versus temperature diagram for $\text{Ni}_{45}\text{Co}_5\text{Mn}_{40}\text{Sn}_{10}$ 1198 K (2 h) furnace cooled ribbons. At low temperatures, the magnetocaloric effect of the martensite is depicted, and at high temperatures, the magnetocaloric effect of austenite is shown. Between 430 K and 443 K, the giant inverse magnetocaloric effect is plotted for the martensite-to-austenite meta-magnetic transition.

microstructure on the magnetocaloric performance of meta-magnetic SMAs.

IV. SUMMARY AND CONCLUSIONS

In summary, we have demonstrated that increasing the grain size to thickness (GS/t) ratio of $\text{Ni}_{45}\text{Mn}_{40}\text{Co}_5\text{Sn}_{10}$ ribbon samples by annealing heat treatments can decrease the magnetic field requirement for magnetic refrigeration by as much as 3 T under the annealing conditions studied. It is expected that the magnitude of field savings can be even larger with further grain growth. Grain growth was promoted more effectively in the range of 1173 to 1198 K, rather than at 1073 K. With increasing the annealing temperature, the distribution of grain sizes also increased, indicating that the grains did not grow uniformly. Nevertheless, the average grain size increased with annealing time and temperature, which decreased the martensite start to finish ($M_s - M_f$) transition range due to reduction in the density of interfaces. The $A_f - A_s$ transition range for the austenite, on the other hand, did not exhibit a significant trend. Decreasing $M_s - M_f$ also decreased $A_f - M_f$ and thereby improved the refrigeration capabilities of the $\text{Ni}_{45}\text{Mn}_{40}\text{Co}_5\text{Sn}_{10}$ by making the structural transformation between paramagnetic austenite and non-magnetic martensite more attainable with smaller fields.

Further grain growth with longer annealing times should continue to reduce the needed magnetic field levels. In this study, the grains did not grow to diameters much larger than the ribbon thickness with the 2 h annealing duration. It is believed, however, that longer annealing times at 1198 K will further increase the grain size and result in a further reduction in the required field levels.

After growing a ribbon with the largest achievable grain size through annealing at 1198 K for 2 h, the giant inverse magnetocaloric effect was experimentally quantified and then compared to theoretical calculations. Although

differential scanning calorimetry demonstrated that the total multiferroic entropy change in $\text{Ni}_{45}\text{Co}_5\text{Mn}_{40}\text{Sn}_{10}$ can be as large as $45 \text{ J kg}^{-1} \text{ K}^{-1}$, only $27 \text{ J kg}^{-1} \text{ K}^{-1}$ was generated with magnetic fields up to 7 T. Melt spun ribbons of the same composition that exhibit a higher degree of grain constraint, i.e. ($GS/t < 1$), are further limited in their magnetic field induced entropy change as they would require even larger magnetic fields to complete the magnetic-field induced martensitic transformation. Further annealing must be performed on melt-spun ribbons and bulk samples in paramagnetic and ferromagnetic MMSMA systems to identify if the grain constraint can be reduced further ultimately leading to a smaller magnetic field requirement for magnetocaloric application of this meta-magnetic shape memory alloy.

ACKNOWLEDGMENTS

This work was supported by the U.S. National Science Foundation, Division of Materials Research, Metals and Metallic Nanostructures Program, Grant Nos. 1108396 and 1508634. In addition, partial support from the National Science Foundation, under Grant No. DMR 08-44082, is acknowledged, which funds research in the International Materials Institute for Multi-functional Materials for Energy Conversion (IIMEC) at Texas A&M University. Y. I. Chumlyakov acknowledges the support from RFBR under Grant No. 12-08-9131-NNIO_a.

- ¹T. Krenke, E. Duman, M. Acet, E. F. Wassermann, X. Moya, L. Manosa, and A. Planes, *Nat. Mater.* **4**, 450 (2005).
- ²E. Bruck, *J. Phys. D: Appl. Phys.* **38**, R381 (2005).
- ³A. Planes, L. Manosa, and M. Acet, *J. Phys.: Condens. Matter* **21**, 23 (2009).
- ⁴X. Moya, S. Kar-Narayan, and N. D. Mathur, *Nat. Mater.* **13**, 439 (2014).
- ⁵J. Liu, T. Gottschall, K. P. Skokov, J. D. Moore, and O. Gutfleisch, *Nat. Mater.* **11**, 620 (2012).
- ⁶V. Provenzano, A. J. Shapiro, and R. D. Shull, *Nature* **429**, 853 (2004).
- ⁷A. M. Tishin and Y. I. Spichkin, *The Magnetocaloric Effect and its Applications* (CRC Press, 2003).
- ⁸R. Kainuma, Y. Imano, W. Ito, Y. Sutou, H. Morito, S. Okamoto, O. Kitakami, K. Oikawa, A. Fujita, T. Kanomata, and K. Ishida, *Nature* **439**, 957 (2006).
- ⁹M. Acet and E. F. Wassermann, *Adv. Eng. Mater.* **14**, 523 (2012).
- ¹⁰J. H. Chen, N. M. Bruno, I. Karaman, Y. J. Huang, J. G. Li, and J. H. Ross, *J. Appl. Phys.* **116**, 203901 (2014).
- ¹¹H. Funakubo and J. B. Kennedy, *Shape Memory Alloys* (Gordon and Breach, 1987).
- ¹²C. Tong and M. Wayman, *Acta Metall.* **22**, 887 (1974).

- ¹³M. Cohen and R. J. Salzbrenner, *Acta Metall. Mater.* **27**, 739 (1978).
- ¹⁴R. Zarnetta, R. Takahashi, M. L. Young, A. Savan, Y. Furuya, S. Thienhaus, B. Maaß, M. Rahim, J. Frenzel, H. Brunken, Y. Chu, V. Srivastava, R. D. James, I. Takeuchi, G. Eggeler, and A. Ludwig, *Adv. Funct. Mater.* **20**, 1917 (2010).
- ¹⁵R. Delville, H. Shi, R. D. James, and D. Schryvers, *Solid State Phenom.* **172–174**, 105 (2011).
- ¹⁶Y. Song, X. Chen, V. Dabade, T. W. Shield, and R. D. James, *Nature* **502**, 85 (2013).
- ¹⁷B. Kockar, I. Karaman, A. Kulkarni, Y. Chumlyakov, and I. V. Kireeva, *J. Nucl. Mater.* **361**, 298 (2007).
- ¹⁸J. Muntassel, J. L. Tamarit, J. M. Guilemany, J. Gil, and E. Cesari, *Mater. Res. Bull.* **23**, 1585 (1988).
- ¹⁹A. Planes, L. Manosa, E. Vives, J. Rodriguez-Carvajal, M. Morin, G. Guenin, and J. L. Macqueron, *J. Phys.: Condens. Matter* **4**, 553 (1992).
- ²⁰J. Liu, T. G. Woodcock, N. Scheerbaum, and O. Gutfleisch, *Acta Mater.* **57**, 4911 (2009).
- ²¹D. Y. Cong, S. Roth, and L. Schultz, *Acta Mater.* **60**, 5335 (2012).
- ²²N. M. Bruno, C. Yegin, I. Karaman, J. H. Chen, J. H. Ross, J. Liu, and J. G. Li, *Acta Mater.* **74**, 66 (2014).
- ²³P. J. Shamberger and F. S. Ohuchi, *Phys. Rev. B* **79**, 144407 (2009).
- ²⁴M. Ahlers, R. Pascual, R. Rapacioli, and W. Arneodo, *Mater. Sci. Eng.* **27**, 49 (1977).
- ²⁵W. Ito, M. Nagasako, R. Y. Umetsu, R. Kainuma, T. Kanomata, and K. Ishida, *Appl. Phys. Lett.* **93**, 232503 (2008).
- ²⁶J. A. Monroe, J. E. Raymond, X. Xu, M. Nagasako, R. Kainuma, Y. I. Chumlyakov, R. Arroyave, and I. Karaman, *Acta Mater.* **101**, 107 (2015).
- ²⁷V. Sanchez-Alarcos, J. I. Perez-Landazabal, V. Recarte, I. Lucia, J. Velez, and J. A. Rodriguez-Velamazan, *Acta Mater.* **61**, 4676 (2013).
- ²⁸Y. Zhang, L. Zhang, Q. Zheng, X. Zheng, M. Li, J. Du, and Y. Aru, *Sci. Rep.* **5**, 11010 (2015).
- ²⁹W. M. Yuhasz, D. L. Schlagel, Q. Xing, R. W. McCallum, and T. A. Lograsso, *J. Alloys Compd.* **492**, 681 (2010).
- ³⁰Mention of commercial equipment is provided only for completely specifying the experimental conditions. It does not imply recommendation or endorsement by the authors or their institutions.
- ³¹V. Srivastava, X. A. Chen, and R. D. James, *Appl. Phys. Lett.* **97**, 014101 (2010).
- ³²I. Dvorak and E. B. Hawbolt, *Metall. Trans.* **6**, 95 (1975).
- ³³M. Somerday, R. J. Comstock, and J. A. Wert, *Metall. Mater. Trans. A* **28**, 2335 (1997).
- ³⁴M. K. Chattopadhyay, V. K. Sharma, and S. B. Roy, *Appl. Phys. Lett.* **92**, 022503 (2008).
- ³⁵L. Caron, Z. Q. Ou, T. T. Nguyen, D. T. Cam Thanh, O. Tegus, and E. Bruck, *J. Magn. Magn. Mater.* **321**, 3559 (2009).
- ³⁶M. Bratko, K. Morrison, A. de Campos, S. Gama, L. F. Cohen, and K. G. Sandeman, *Appl. Phys. Lett.* **100**, 252409 (2012).
- ³⁷J. Ortin and A. Planes, *Acta Metall. Mater.* **36**, 1873 (1988).
- ³⁸C. M. Wayman and H. C. Tong, *Scr. Metall. Mater.* **11**, 341 (1977).
- ³⁹Y. Sutou, Y. Imano, N. Koeda, T. Omori, R. Kainuma, K. Ishida, and K. Oikawa, *Appl. Phys. Lett.* **85**, 4358 (2004).
- ⁴⁰J.-H. Chen, N. M. Bruno, I. Karaman, Y. Huang, J. Li, and J. H. Ross, Jr., *Acta Mater.* **105**, 176 (2016).
- ⁴¹M. Vadala, Ph.D. Dissertation (Ruhr University, 2008).
- ⁴²N. M. Bruno, Ph.D. Dissertation (Texas A&M University, 2015).